host (as indeed we find from first-principles calculations). But these formation energies are related in the following fashion.

Our key quantity is $\varepsilon(+/-)$, the Fermi-level position where H^+ and H^- have equal formation energy. In the model, this occurs when the Fermi level is located midway between db_C and db_A. Indeed, to form H^+ we need to remove an electron from db_C; and to form H^- we need to place an electron in db_A. The location of E_F halfway between db_C and db_A corresponds to the 'charge neutrality' level that has been extensively discussed in the literature[21]. Indeed, it is well established that the charge neutrality level can be used to line up semiconductor band structures. If $\varepsilon(+/-)$ coincides with the charge neutrality level, then the alignment of $\varepsilon(+/-)$ in accordance with band line-ups follows directly from the established use of the charge neutrality level for this purpose. A crucial feature is that, within this model, the strengths of the individual H–C and H–A bonds (which are highly material dependent) do not enter into the determination of $\varepsilon(+/-)$. We note that, being a localized deep level, db_C is related to conduction-band states derived from the entire Brillouin zone, and not directly tied to the position of the CBM, which reflects only a single point in the zone. Similarly the db_A state is distinct from the VBM. This explains why $\varepsilon(+/-)$ can fall outside the bandgap.

We point out that the energetic position of $\varepsilon(+/-)$ on our absolute energy scale is about 4.5 eV below the vacuum level. This value is remarkably similar to an important quantity in electrochemistry, namely the chemical potential for electrons under 'standard hydrogen electrode' (SHE) conditions, which is at −4.44 eV referenced to the vacuum level (see Fig. 2). This is not a coincidence. The 'normal' or 'standard' hydrogen electrode refers to an H^+(aq.)/H_2(g) electrode in water. In the framework of the present study, the relevant reaction is viewed as formation of H^+ (with H_2 as the reservoir) in an H_2O host. The equivalent of the $\varepsilon(+/-)$ level for this system can be estimated on the basis of formation energies of hydrated H_3O^+ and OH^- (refs 22, 23), resulting in a $\varepsilon(+/-)$ value between −4.2 and −4.5 eV (reflecting the spread in values for hydration enthalpies), in satisfactory agreement with the potential of the SHE. This alignment, included in Fig. 2, allows a direct connection to an important problem in electrochemistry, namely the prediction of band-edge positions of semiconductors and insulators in contact with water[24].

More generally, we have observed that $\varepsilon(+/-)$ levels based on proton affinities and deprotonation energies[22] for a wide range of molecules fall within a narrow range. Dielectric screening, which is implicitly present in a liquid environment and plays a central role in the charge neutrality level[21], narrows this range even further. The fact that the universality of the alignment extends to aqueous solutions highlights the commonality of driving forces for hydrogen chemistry across a wide range of systems. □

Methods

The calculations for interstitial H were performed in supercells containing either 64 atoms for zinc blende or 96 atoms for wurtzite. Effects of semicore *d* states (such as the 3*d* states in Ga or Zn) were included using the nonlinear core correction[11]. For H the Coulomb potential is used. Energy differences for hydrogen-containing systems are well converged at a 40-Ry plane-wave cut-off. For each charge state of H, many possible sites in the lattice were explored and the global minimum was identified. We estimate the error bar on $\varepsilon(+/-)$ due to DFT-LDA errors to be ~0.4 eV, based on comparisons between calculations with different pseudopotentials (particularly those that result in different bandgaps owing to different treatments of the semicore *d* states). The bandgap error inherent in DFT-LDA has only minor effects on $\varepsilon(+/-)$, because the formation energies of H^+ and H^- are not sensitive to bandgap corrections: for H^+, the defect-induced state is unoccupied, whereas for H^-, the state is related to an anion dangling bond and thus valence-band derived. Calculations for band line-ups were performed for nonpolar interfaces using the methodology of ref. 12. The line-up for Si/SiO_2 was taken from ref. 25.

Received 29 November 2002; accepted 24 April 2003; doi:10.1038/nature01665.

1. Pankove, J. I. & Johnson, N. M. *Semiconductors and Semimetals* Vol. 34, *Hydrogen in Semiconductors* (Boston, Academic, 1991).
2. Blöchl, P. & Stathis, J. H. Hydrogen electrochemistry and stress-induced leakage current in silica. *Phys. Rev. Lett.* **62,** 372–375 (1999).
3. Schlapbach, L. & Züttel, A. Hydrogen-storage materials for mobile applications. *Nature* **414,** 353–358 (2001).
4. Mills, B. E., Martin, R. L. & Shirley, D. A. Further studies of the core binding energy-proton affinity correlation in molecules. *J. Am. Chem. Soc.* **98,** 2380–2385 (1976).
5. Van de Walle, C. G. & Johnson, N. M. in *Semiconductors and Semimetals* Vol. 57, *Gallium Nitride (GaN) II* (eds Pankove, J. I. & Moustakas, T. D.) 157–184 (Academic, Boston, 1998).
6. Van de Walle, C. G. Hydrogen as a cause of doping in ZnO. *Phys. Rev. Lett.* **85,** 1012–1015 (2000).
7. Hofmann, D. M. *et al.* Hydrogen: a relevant shallow donor in zinc oxide. *Phys. Rev. Lett.* **88,** 045504 (2002).
8. Limpijumnong, S. & Van de Walle, C. G. Passivation and doping due to hydrogen in III-nitrides. *Phys. Status Solidi B* **228,** 303–307 (2001).
9. Franciosi, A. & Van de Walle, C. G. Heterojunction band offset engineering. *Surf. Sci. Rep.* **25,** 1–140 (1996).
10. Bockstedte, M., Kley, A., Neugebauer, J. & Scheffler, M. Density-functional theory calculations for poly-atomic systems: Electronic structure, static and elastic properties and *ab initio* molecular dynamics. *Comput. Phys. Commun.* **107,** 187–222 (1997).
11. Louie, S. G., Froyen, S. & Cohen, M. L. Nonlinear ionic pseudopotentials in spin-density-functional calculations. *Phys. Rev. B* **26,** 1738–1742 (1982).
12. Van de Walle, C. G. & Martin, R. M. Theoretical calculations of heterojunction discontinuities in the Si/Ge system. *Phys. Rev. B* **34,** 5621–5634 (1986).
13. Van de Walle, C. G. Band lineups and deformation potentials in the model-solid theory. *Phys. Rev. B* **39,** 1871–1883 (1989).
14. Majewski, J. A., Städele, M. & Vogl, P. Stability and band offsets of SiC/GaN, SiC/AlN, and AlN/GaN heterostructures. *Mater. Res. Soc. Symp. Proc.* **449,** 917–922 (1997).
15. Yu, E. T., McCaldin, J. O. & McGill, T. C. in *Solid State Physics* Vol. 46 (eds Ehrenreich, H. & Turnbull, D.) 1–146 (Academic, Boston, 1992).
16. Look, D. C. *et al.* Donor and acceptor concentrations in degenerate InN. *Appl. Phys. Lett.* **80,** 258–260 (2002).
17. Janotti, A., Zhang, S. B., Wei, S.-H. & Van de Walle, C. G. The effects of hydrogen on the electronic properties of GaAsN alloys. *Phys. Rev. Lett.* **89,** 086403 (2002).
18. Ledebo, L. Å. & Ridley, B. K. On the position of energy levels related to transition-metal impurities in III-V semiconductors. *J. Phys. C* **15,** L961–L964 (1982).
19. Caldas, M. J., Fazzio, A. & Zunger, A. A universal trend in the binding energies of deep impurities in semiconductors. *Appl. Phys. Lett.* **45,** 671–673 (1984).
20. Tersoff, J. & Harrison, W. A. Transition-metal impurities in semiconductors — their connection with band lineups and Schottky barriers. *Phys. Rev. Lett.* **58,** 2367–2370 (1987).
21. Tersoff, J. Theory of semiconductor heterojunctions: The role of quantum dipoles. *Phys. Rev. B* **30,** 4874–4877 (1984).
22. NIST Chemistry WebBook ⟨http://webbook.nist.gov/chemistry⟩ (March 2003).
23. Mejias, J. A. & Lago, S. Calculation of the absolute hydration enthalpy and free energy of H^+ and OH^-. *J. Chem. Phys.* **113,** 7306–7316 (2000).
24. Grätzel, M. Photoelectrochemical cells. *Nature* **414,** 338–344 (2001).
25. Tuttle, B. R. *Ab initio* valence band offsets between Si(100) and SiO_2 from microscopic models. *Phys. Rev. B* **67,** 155324 (2003).

Acknowledgements We thank S. Limpijumnong, M. Fuchs, M. Chabinyc, D. Biegelsen and the late J. McCaldin for discussions and support. This work was supported in part by the Air Force Office of Scientific Research and by the Deutsche Forschungsgemeinschaft.

Competing interests statement The authors declare that they have no competing financial interests.

Correspondence and requests for materials should be addressed to C.G.V.d.W. (vandewalle@parc.com).

Chaperonin-mediated stabilization and ATP-triggered release of semiconductor nanoparticles

Daisuke Ishii*, Kazushi Kinbara*, Yasuhiro Ishida*, Noriyuki Ishii†, Mina Okochi‡, Masafumi Yohda‡ & Takuzo Aida*

** Department of Chemistry and Biotechnology, School of Engineering, The University of Tokyo, 7-3-1 Hongo, Bunkyo-ku, Tokyo 113-8656, Japan*
† Biological Information Research Center, National Institute of Advanced Industrial Science and Technology, Tsukuba Central 6, 1-1-1 Higashi, Tsukuba, Ibaraki 305-8566, Japan
‡ Department of Biotechnology, Faculty of Technology, Tokyo University of Agriculture and Technology, 2-24-16 Naka-cho, Koganei, Tokyo 184-8588, Japan

Various properties of semiconductor nanoparticles, including photoluminescence and catalytic activity, make these materials attractive for a range of applications[1,2]. As nanoparticles readily coagulate and so lose their size-dependent properties, shape-persistent three-dimensional stabilizers that enfold nanoparti-

cles have been exploited[3–9]. However, such wrapping approaches also make the nanoparticles insensitive to external stimuli, and so may limit their application. The chaperonin proteins GroEL (from *Escherichia coli*) and *T.th* ('*T.th* cpn', from *Thermus thermophilus* HB8) encapsulate denatured proteins inside a cylindrical cavity; after refolding, the encapsulated proteins are released by the action of ATP inducing a conformational change of the cavity[10,11]. Here we report that GroEL and *T.th* cpn can also enfold CdS semiconductor nanoparticles, giving them high thermal and chemical stability in aqueous media. Analogous to the biological function of the chaperonins, the nanoparticles can be readily released from the protein cavities by the action of ATP. We expect that integration of such biological mechanisms into materials science will open a door to conceptually new bio-responsive devices.

The chaperonin GroEL consists of two supramolecular rings that are stacked to form a double-decker architecture (Fig. 1a)[12]. (Each ring consists of seven protein subunits; each subunit has a molecular mass of 60 kDa.) GroEL possesses a cylindrical cavity with a diameter of 4.5 nm, and a wall thickness of 4.6 nm (ref. 13). The chaperonin *T.th* cpn originates from the thermophilic bacterium, *Thermus thermophilus* HB8[14,15], and consists of a GroEL-like tetradecamer (840 kDa) of a protein subunit called cpn60 (60 kDa), which is hybridized, with a capping protein assembly $[cpn10]_7$ (70 kDa) on either side of its cylindrical cavity (Fig. 1a)[16,17]. Transmission electron microscopy (TEM) showed that the cavity size and wall thickness of *T.th* cpn (~5 nm) are both comparable to those of GroEL.

We prepared CdS nanoparticles (2–4 nm) according to a method reported in ref. 18. For the complexation with chaperonins, a dimethylformamide (DMF) solution of CdS nanoparticles was added to a Tris–HCl buffer solution of GroEL or *T.th* cpn. In the presence of the chaperonin proteins, the photoluminescence of CdS nanoparticles at 430–720 nm (excitation wavelength $\lambda_{ext} = 370$ nm) lasted for an unusually long period of time without decay (for example, 400 days with GroEL). In the absence of the chaperonins, the characteristic fluorescence disappeared within 2 hours.

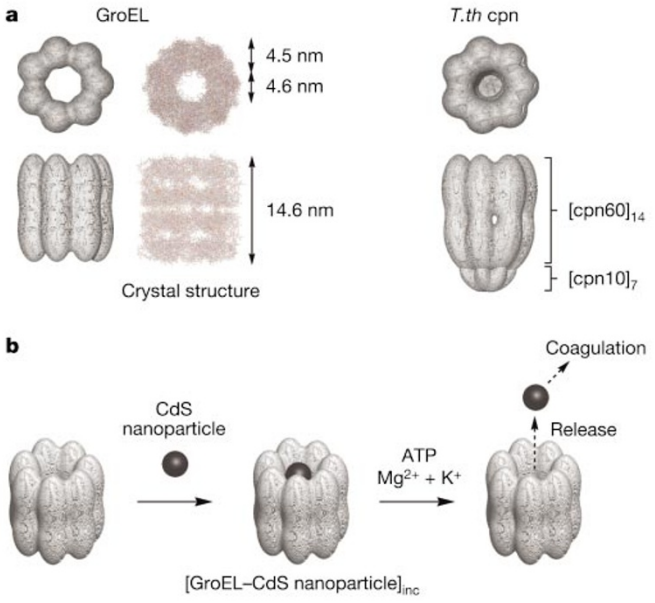

Figure 1 Chaperonin proteins as ATP-responsive barrels for inclusion of nanoparticles. **a**, Schematic illustrations (top and side views) of GroEL (crystal structures, right)[13] and *T.th* cpn. **b**, Schematic representation of the formation of GroEL–CdS nanoparticle complexes by inclusion of CdS nanoparticles into the cylindrical cavity of GroEL, and its ATP-triggered guest release.

The tubular structure of the chaperonin proteins was essential for the stabilization of CdS nanoparticles. Fluorescence was not enhanced by the use of GroES, a bowl-shaped, $[cpn10]_7$-like GroEL-capping protein, in place of GroEL.

We isolated complexes of *T.th* cpn or GroEL with CdS nanoparticles by size-exclusion chromatography (SEC). By means of inductively coupled plasma mass spectrometry (ICP-MS), we confirmed that the complexes both contained Cd^{2+}. The *T.th* cpn–nanoparticle complex showed circular dichroism bands, whose intensities were identical to those of intact *T.th* cpn. An analytical SEC trace of this solution with an ultraviolet (UV)/fluorescence dual detector showed single, sharp elution peaks, which were superimposable with one another at nearly the same elution volume as intact *T.th* cpn (Fig. 2a). As intact *T.th* cpn is barely fluorescent, the above results strongly indicate that the CdS nanoparticles co-localized with *T.th* cpn to form an inclusion complex. The photoluminescence of the complexes at 430–720 nm upon excitation at 370 nm is characteristic of CdS nanoparticles (Supplementary Fig. S1)[19,20]. We also conducted analytical SEC of the *T.th* cpn–CdS inclusion complexes using a refractive index (RI)/multi-angle light scattering dual detector, where the molecular mass of the complex was evaluated to be 915 ± 4 kDa, which is nearly identical to that of intact *T.th* cpn (910 kDa) (Supplementary Fig. S2). These results demonstrate that *T.th* cpn within the protein–nanoparticle complex preserves its own structural identity, without formation of higher aggregates or dissociation into the protein subunits.

We also succeeded in imaging these complexes by TEM. Figure 3a shows a TEM picture of the *T.th* cpn–CdS inclusion complex, isolated by SEC and stained with uranyl acetate, where the bullet-like side view and the doughnut-like end-on view of *T.th* cpn protein are clearly observed, as reported previously[16,17]. The TEM picture of the *T.th* cpn–CdS inclusion complex in the end-on orientation shows a darker central region when compared to intact *T.th* cpn (Fig. 3c, Supplementary Fig. S4), owing to the presence of a CdS nanoparticle within the protein cavity (Fig. 3b). No CdS nanoparticles were observed on the exterior of the protein surface. When a single inclusion complex was irradiated for 1 minute by a focused electron beam, the protein was partially destroyed, so that the CdS nanoparticle included within the chaperonin cavity was more clearly imaged by TEM (Supplementary Fig. S3). From the TEM image under such partially destructive conditions, only a single nanoparticle appeared to be present within the chaperonin cavity. As the CdS nanoparticles are positively charged owing to Cd^{2+} ions on the surface, it is reasonable to conclude that a second nanoparticle will not be included in the chaperonin cavity owing to electrostatic repulsion. For statistical analysis of the TEM picture, we randomly selected 793 images of end-on *T.th* cpn–CdS nanoparticle complexes, and found that 75% showed a dark central cavity due to the presence of a CdS nanoparticle.

The CdS nanoparticles within the chaperonin proteins are electronically insulated. The photoexcited singlet state of CdS nanoparticles is known to be quenched by an electron acceptor such as methyl viologen (MV^{2+}) via photoinduced electron transfer from the former to the latter[21,22]. Fluorescence titration of CdS nanoparticles in DMF with MV^{2+} at 25 °C gave Stern–Volmer plots (Fig. 4), from which the Stern–Volmer constant was evaluated to be 3.3. In sharp contrast, the fluorescence quenching of the inclusion complex with GroEL took place much less efficiently even at a high concentration of MV^{2+}, where the observed Stern-Volmer constant (0.20) was more than 15 times smaller than that for intact CdS nanoparticles. We also found an even smaller Stern–Volmer constant for the *T.th* cpn–nanoparticle complex (0.09). These observations are quite reasonable, considering that the thickness of the protein envelope around the CdS nanoparticle (4.6 nm for GroEL[13]) exceeds an upper limit of the electron-transferable distance (~3 nm) in ordinary systems.

Chaperonins belong to the family of heat-shock proteins[23], and

T.th cpn, originating from a thermophilic bacterium, has been reported to be stable against thermal denaturation up to 80 °C (ref. 14). We found that the *T.th* cpn–CdS nanoparticle complex is also thermally stable, and maintains its characteristic photoluminescence activity up to 80 °C. In heating–cooling cycles in a temperature range of 4–80 °C (Fig. 5a), the photoluminescence of the inclusion complex in Tris–HCl buffer was quenched upon heating, but recovered the original intensity upon cooling down to 4 °C. However, when heated at 90 °C for 10 min, the protein component underwent partial denaturation as observed by circular dichroism, and the complex irreversibly lost 18% of its photoluminescence activity (Fig. 5a, arrow). Although intact CdS nanoparticles in DMF also showed a similar temperature-dependent photoluminescence profile, the response became irreversible upon heating at only 30 °C, forming a colloidal precipitate of CdS. A GroEL–CdS nanoparticle complex showed thermoresponsive photoluminescence activity (Fig. 5b), but became partially irreversible upon heating for 20 min at 60 °C (Fig. 5b, arrow), just below the denaturation temperature of intact GroEL[24]. Thus, the thermal stability of the included nanoparticle is totally dependent on that of the chaperonin protein.

Chaperonin proteins, upon binding with ATP in the presence of Mg^{2+} and K^{+}, undergo a large conformational change, which results in the release of refolded guest proteins from the cavity[25,26]. We found that *T.th* cpn–CdS nanoparticle complexes also respond to ATP, and release included nanoparticles from the cavities under similar conditions (Fig. 1b). When a Tris–HCl buffer solution of ATP containing $MgCl_2$ was added to a buffer solution of *T.th* cpn–CdS nanoparticle complexes containing KCl, the mixture turned slightly cloudy within seconds to give colloidal substances, where the supernatant solution after centrifugation was no longer fluorescent (Fig. 2c). The release of CdS nanoparticles from *T.th* cpn complexes by the action of ATP was clearly demonstrated by analytical SEC with a UV/fluorescence dual detector (Fig. 2b). After the addition of ATP, the UV response of the SEC trace of the complexes showed a sharp elution peak assignable to *T.th* cpn and an additional broad peak in the lower-molecular-mass region due to ATP and its hydrolysed products, while no fluorescence responses

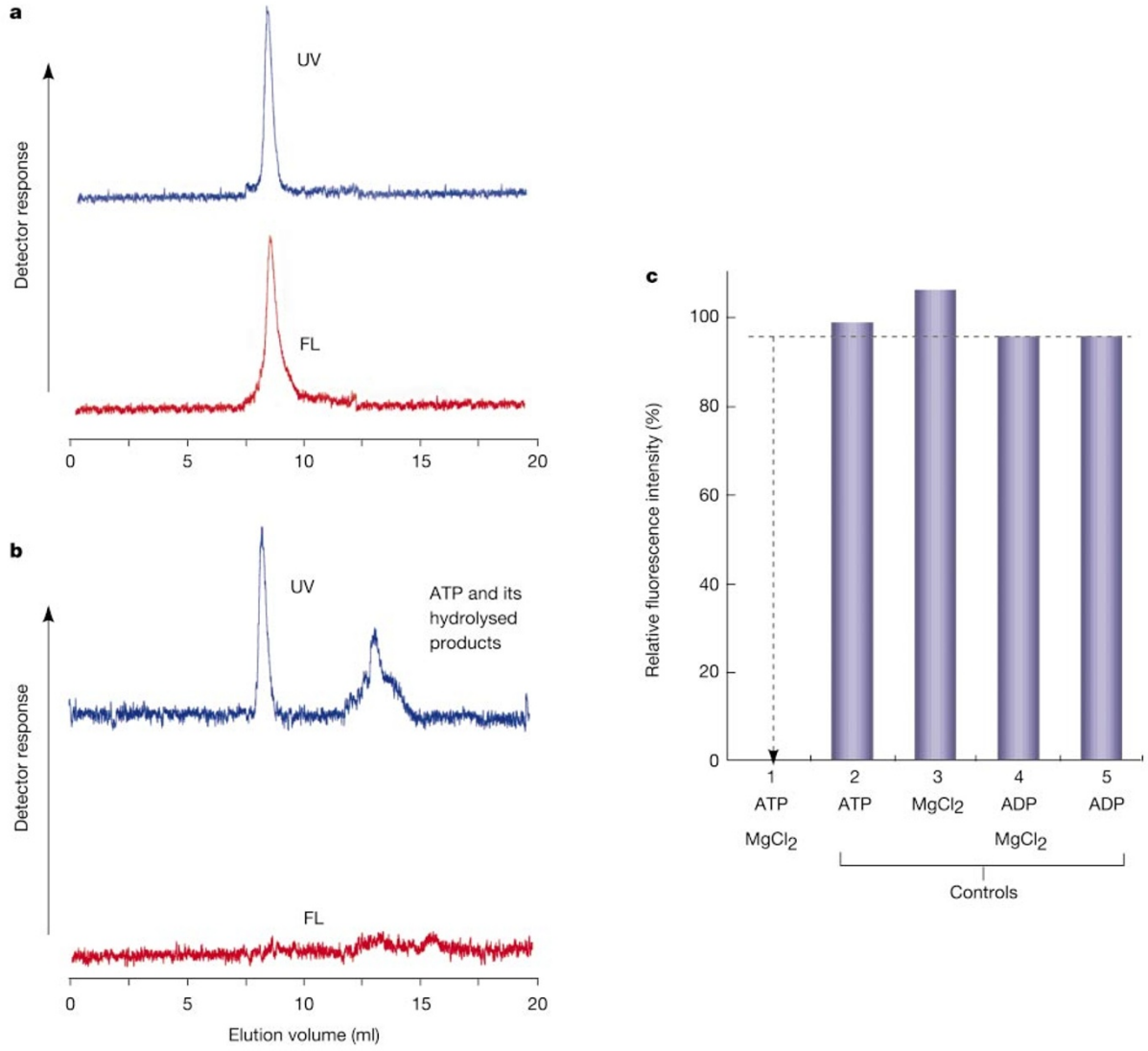

Figure 2 SEC analysis of *T.th* cpn–CdS the nanoparticle inclusion complex and its specific response to ATP in KCl-containing Tris–HCl buffer. **a**, Analytical SEC trace of *T.th* cpn–CdS inclusion complexes monitored by an UV (upper chart)/fluorescence (FL) (lower chart) dual detector, and **b**, that of *T.th* cpn–CdS inclusion complexes after addition of ATP and $MgCl_2$. The peak at 12.5–15.0 ml is derived from ATP and its hydrolysed products. **c**, Changes in fluorescence intensity of *T.th* cpn–CdS complexes in Tris–HCl buffer: 1, ATP + $MgCl_2$; 2, ATP; 3, $MgCl_2$; 4, ADP + $MgCl_2$; 5, ADP.

were observed for these two peaks. The fraction corresponding to *T.th* cpn, isolated by SEC from the reaction mixture, lost most (nearly 90%) of its Cd^{2+}, as determined by ICP-MS. On the other hand, addition of ATP or $MgCl_2$ alone to the KCl-containing buffer solution of the inclusion complexes neither resulted in the generation of colloidal substances nor fluorescence quenching (Fig. 2c)—in contrast, a DMF solution of intact CdS nanoparticles immediately lost its luminescence activity upon addition of $MgCl_2$.

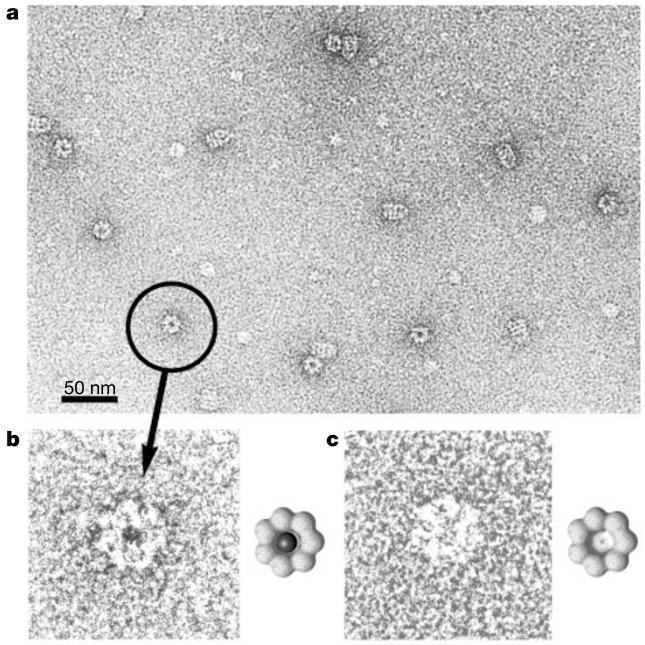

Figure 3 Transmission electron micrographs of *T.th* cpn–CdS nanoparticle complexes and intact *T.th* cpn. **a**, **b**, *T.th* cpn–CdS nanoparticle complexes isolated by SEC. **c**, Intact *T.th* cpn. The models on the right sides of the images in **b** and **c** are schematic representations of the end-view of the complex and intact *T.th* cpn, respectively.

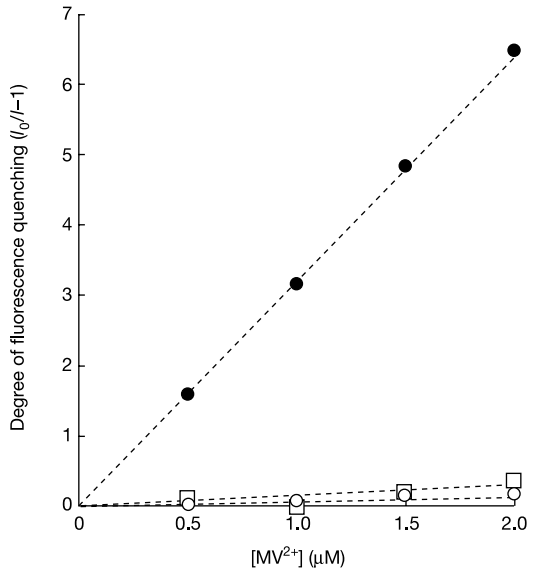

Figure 4 Shielding effects of chaperonins on electron transfer from CdS nanoparticles to methyl viologen (MV^{2+}). Stern–Volmer plots for fluorescence titration with MV^{2+} at 25 °C of a DMF solution of CdS nanoparticle (filled circles), a Tris–HCl buffer solution containing GroEL–CdS nanoparticle inclusion complexes (open squares), and a Tris–HCl buffer solution of *T.th* cpn–CdS nanoparticle inclusion complexes (open circles). I and I_0 represent the intensities of fluorescence and its initial value, respectively.

Thus, *T.th* cpn makes the included CdS nanoparticle thermally stable, tolerant to electrolytes, and electronically dormant, but can readily release the guest nanoparticle from its cylindrical cavity upon binding with ATP. As expected, the *T.th* cpn–CdS nanoparticle complexes hardly responded to ADP (adenosine-5′-diphosphate)—there was no substantial change in the fluorescence intensity, regardless of the presence or absence of Mg^{2+} (Fig. 2c). We also found that GroEL–CdS nanoparticle complexes behave similarly upon binding with ATP. □

Methods

Sample preparation

To a N_2-purged DMF solution of $Cd(OAc)_2{\cdot}2H_2O$ (30 ml, 5.56 mM), with vigorous stirring, was added dropwise a MeOH solution of $Na_2S{\cdot}9H_2O$ (3 ml, 5.56 mM) at −40 °C. The resulting mixture was stirred for 1.5 h to afford a yellow solution, which showed absorption and emission spectra ($\lambda_{ext} = 370$ nm, emission wavelength $\lambda_{em} = 530$ nm) characteristic of nanosized CdS particles. TEM analysis showed that the resulting CdS nanoparticles have a size distribution in which the majority were in the diameter range 2–4 nm. To a 1.9-ml Tris–HCl buffer (25 mM, pH 7.5 with 100 mM KCl) solution of *T.th* cpn (0.5 μM) was added dropwise a 100-μl DMF solution of CdS nanoparticles (5.56 mM based on Cd^{2+}) at 4 °C. The mixture was allowed to stand at 4 °C until the initial spectral change subsided (~100 h), and then subjected to SEC using Tris–HCl buffer (25 mM, pH 7.5 with 100 mM KCl) as eluent on Sephacryl S-300 HR or S-400 HR with an ÄKTA-prime low-pressure chromatography system (Amersham Pharmacia Biotech). SEC traces at 280 nm allowed the isolation of a protein-containing fraction, which was concentrated by ultrafiltration with an USY-5 ultrafilter unit (Advantec) at 4 °C, affording 2 ml of a Tris–HCl buffer solution of the *T.th* cpn–CdS nanoparticle complex (0.1 μM). Preparation and isolation of GroEL–CdS nanoparticle inclusion complexes were performed in a similar fashion.

Characterization

Analytical SEC traces (TSK gel G4000SW_{XL} (Tosoh); eluent, Tris–HCl buffer 25 mM, pH 7.5 with 100 mM KCl) of *T.th* cpn–CdS nanoparticle inclusion complexes were followed by UV (observed at 280 nm) and fluorescence (excitation at 370 nm, observed at 530 nm) responses by UV970 and FP2020-plus spectrophotometers (JASCO), respectively, at a flow rate of 0.5 ml min^{-1}. Analytical SEC (Tosoh TSK gel G4000SW_{XL} or Shodex Protein KW-804) of the complexes was performed using an UV/fluorescence dual detector and an RI/multi-angle light scattering dual detector, at a flow rate of 0.5 ml min^{-1}.

TEM imaging

Samples were applied to an electron microscope specimen grid covered with a thin carbon support film that had been hydrophilized by ion bombardment. After drying with a pre-water-soaked filter paper, the grid was negatively stained with 1% uranyl acetate. TEM micrographs were then recorded on a JEM-2010 TEM (JEOL) operating at an anode voltage of 120 kV.

Methyl viologen titration

To a DMF solution of CdS nanoparticles (2 ml, 700 nM based on Cd^{2+}) were added 10-μl aliquots of a 100-μM Tris–HCl buffer (25 mM, pH 7.5 with 100 mM KCl) solution of

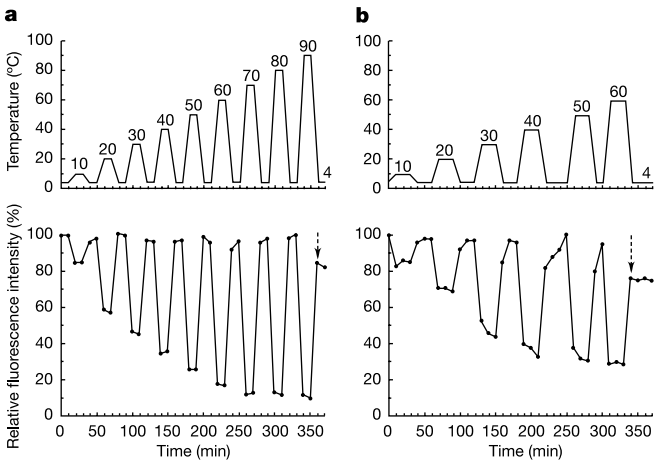

Figure 5 Thermal stabilities and relative fluorescence intensities of GroEL–CdS and *T.th* cpn–CdS inclusion complexes. Top, temperature-dependent photoluminescence profiles of **a**, *T.th* cpn–CdS and **b**, GroEL–CdS nanoparticle inclusion complexes in Tris–HCl buffer. Fluorescence intensities at 4 °C were used as the bases for relative fluorescence intensities (bottom). Numbers of plateau in top panels denote annealing temperatures.

MV^{2+}. Likewise, Tris–HCl buffer (25 mM, pH 7.5 with 100 mM KCl) solutions of GroEL–CdS complex and *T.th* cpn–CdS complex (2 ml, 700 nm based on Cd^{2+}) were titrated. Emission ($\lambda_{ext} = 370$ nm) spectra were recorded on a FP-777W spectrophotometer (JASCO).

Thermal stability

Fluorescence spectra ($\lambda_{ext} = 370$ nm, wavelength of observed fluorescence $\lambda_{obsd} = 530$ nm) of GroEL–CdS complexes and *T.th* cpn–CdS complexes were recorded at designated temperatures on a FP-777W spectrophotometer (JASCO), where the fluorescence intensities at 4 °C were used as the bases for relative fluorescence intensities. The temperature was directly controlled by a ECT271 Peltier thermometric apparatus (JASCO; 40 °C min^{-1} on heating and 25 °C min^{-1} on cooling).

ATP response

To a 2-ml Tris–HCl buffer (25 mM, pH 7.5 with 100 mM KCl) solution of *T.th* cpn–CdS complexes (0.5 μM based on *T.th* cpn) were added aqueous solutions of ATP (100 mM) and $MgCl_2$ (1 M) ([ATP] = 20 μM, $[Mg^{2+}] = 25$ mM after mixing), and the mixture was incubated at 70 °C for 10 min. The supernatant solution was subjected to fluorescence spectroscopy and analytical SEC with an UV/fluorescence dual detector.

Received 11 November 2002; accepted 14 April 2003; doi:10.1038/nature01663.

1. Alivisatos, A. P. Semiconductor clusters, nanocrystals, and quantum dots. *Science* **271,** 933–937 (1996).
2. Schmid, G. *et al.* Current and future applications of nanoclusters. *Chem. Soc. Rev.* **28,** 179–185 (1999).
3. Meldrum, F. C., Heywood, B. R. & Mann, S. Magnetoferritin — *in vitro* synthesis of a novel magnetic protein. *Science* **257,** 522–523 (1992).
4. Wong, K. K. W. & Mann, S. Biomimetic synthesis of cadmium sulfide-ferritin nanocomposites. *Adv. Mater.* **8,** 928–932 (1996).
5. Shenton, W., Pum, D., Sleytr, U. B. & Mann, S. Biocrystal templating of CdS superlattices using self-assembled bacterial S-layers. *Nature* **389,** 585–587 (1997).
6. Balogh, L. & Tomalia, D. A. Poly(amidoamine) dendrimer-templated nanocomposites. 1. Synthesis of zerovalent copper nanoclusters. *J. Am. Chem. Soc.* **120,** 7355–7356 (1998).
7. Lemon, B. I. & Crooks, R. M. Preparation and characterization of dendrimer-encapsulated CdS semiconductor quantum dots. *J. Am. Chem. Soc.* **122,** 12886–12887 (2000).
8. Shenton, W., Mann, S., Cölfen, H., Bacher, A. & Fischer, M. Synthesis of nanophase iron oxide in lumazine synthase capsids. *Angew. Chem. Int. Edn Engl.* **40,** 442–445 (2001).
9. McMillan, R. A. *et al.* Ordered nanoparticle arrays formed on engineered chaperonin protein templates. *Nature Mater.* **1,** 247–252 (2002).
10. Roseman, A. M., Chen, S., White, H., Braig, K. & Saibil, H. R. The chaperonin ATPase cycle: mechanism of allosteric switching and movements of substrate-binding domains in groEL. *Cell* **87,** 241–251 (1996).
11. Ranson, N. A. *et al.* ATP-bound states of groEL captured by cryo-electron microscopy. *Cell* **107,** 869–879 (2001).
12. Hendrix, R. W. Purification and properties of groE, a host protein involved in bacteriophage assembly. *J. Mol. Biol.* **129,** 375–392 (1979).
13. Braig, K. *et al.* The crystal structure of the bacterial chaperonin groEL at 2.8 Å. *Nature* **371,** 578–586 (1994).
14. Taguchi, H., Konishi, J., Ishii, N. & Yoshida, M. A chaperonin from a thermophilic bacterium, *Thermus thermophilus*, that controls refoldings of several thermophilic enzymes. *J. Biol. Chem.* **266,** 22411–22418 (1991).
15. Amada, K. *et al.* Molecular cloning, expression, and characterization of chaperonin-60 and chaperonin-10 from a thermophilic bacterium, *Thermus thermophilus* HB8. *J. Biochem.* **118,** 347–354 (1995).
16. Ishii, N., Taguchi, H., Sumi, M. & Yoshida, M. Structure of holo-chaperonin studied with electron microscopy. Oligomeric cpn10 on top of two layers of cpn60 rings with two stripes each. *FEBS Lett.* **299,** 169–174 (1992).
17. Ishii, N., Taguchi, H., Sasabe, H. & Yoshida, M. Folding intermediate binds to the bottom of bullet-shaped holo-chaperonin and is readily accessible to antibody. *J. Mol. Biol.* **236,** 691–696 (1994).
18. Murakoshi, K. *et al.* Preparation of size-controlled hexagonal CdS nanocrystallites and the characteristics of their surface structures. *J. Chem. Soc. Faraday Trans.* **94,** 579–586 (1998).
19. Hosokawa, H. *et al. In-situ* EXAFS observation of the surface structure of colloidal CdS nanocrystallites in *N*,*N*-dimethylformamide. *J. Phys. Chem.* **100,** 6649–6656 (1996).
20. Brus, L. E. Electron-electron and electron-hole interactions in small semiconductor crystallites: The size dependence of the lowest excited electronic state. *J. Chem. Phys.* **80,** 4403–4409 (1984).
21. Ramsden, J. J. & Grätzel, M. Photoluminescence of small cadmium sulfide particles. *J. Chem. Soc. Faraday Trans. 1* **80,** 919–933 (1984).
22. Hengleln, A. Photochemistry of colloidal cadmium sulfide. 2. Effects of adsorbed methyl viologen and of colloidal platinum. *J. Phys. Chem.* **86,** 2291–2293 (1982).
23. Llorca, O., Galán, A., Carrascosa, J. L., Muga, A. & Valpuesta, J. M. GroEL under heat-shock. *J. Biol. Chem.* **273,** 32587–32594 (1998).
24. Martin, J., Horwich, A. L. & Hartl, F. U. Prevention of protein denaturation under heat stress by the chaperonin Hsp60. *Science* **258,** 995–998 (1992).
25. Goloubinoff, P., Christeller, J. T., Gatenby, A. A. & Lorimer, G. H. Reconstitution of active dimeric ribulose bisphosphate carboxylase from an unfolded state depends on two chaperonin proteins and Mg-ATP. *Nature* **342,** 884–889 (1989).
26. Todd, M. J., Viitanen, P. V. & Lorimer, G. H. Hydrolysis of adenosine 5′-triphosphate by *Escherichia coli* groEL: effects of groES and potassium ion. *Biochemistry* **32,** 8560–8567 (1993).

Supplementary Information accompanies the paper on **www.nature.com/nature**.

Acknowledgements We thank K. Konishi for his initial contribution to the present work; K. Tsumoto for discussions; J. Oono and M. Nakamura for SEC analysis with MALS. N.I. was responsible for TEM microscopy. We acknowledge support from the 21st Century COE Programs of Research and Education (T.A., Human–Friendly Materials Based on Chemistry; M.Y., Future Nano-Materials), and from the JST ERATO Nanospace program. K.K. acknowledges support from the Nissan Science Foundation.

Competing interests statement The authors declare that they have no competing financial interests.

Correspondence and requests for materials should be addressed to T.A. (aida@macro.t.u-tokyo.ac.jp).

Evidence for low sulphate and anoxia in a mid-Proterozoic marine basin

Yanan Shen*, Andrew H. Knoll* & Malcolm R. Walter†

** Botanical Museum, Harvard University, 26 Oxford Street, Cambridge, Massachusetts 02138, USA*
† Australian Centre for Astrobiology, Macquarie University, New South Wales 2109, Australia

Many independent lines of evidence document a large increase in the Earth's surface oxidation state 2,400 to 2,200 million years ago[1–4], and a second biospheric oxygenation 800 to 580 million years ago, just before large animals appear in the fossil record[5,6]. Such a two-staged oxidation implies a unique ocean chemistry for much of the Proterozoic eon, which would have been neither completely anoxic and iron-rich as hypothesized for Archaean seas, nor fully oxic as supposed for most of the Phanerozoic eon[7]. The redox chemistry of Proterozoic oceans has important implications for evolution[8], but empirical constraints on competing environmental models are scarce. Here we present an analysis of the iron chemistry of shales deposited in the marine Roper Basin, Australia, between about 1,500 and 1,400 million years ago, which record deep-water anoxia beneath oxidized surface water. The sulphur isotopic compositions of pyrites in the shales show strong variations along a palaeodepth gradient, indicating low sulphate concentrations in mid-Proterozoic oceans. Our data help to integrate a growing body of evidence favouring a long-lived intermediate state of the oceans, generated by the early Proterozoic oxygen revolution and terminated by the environmental transformation late in the Proterozoic eon.

The Roper Group is a thick (>1,500 m), predominately marine siliciclastic succession preserved over an area of 145,000 km^2 west of the Gulf of Carpenteria in Australia's Northern Territory. The ramp-like succession, formed in an intracratonic basin in contact with the global ocean, contains six major depositional sequences that record episodic flooding followed by basin filling and shoreline progradation[9]. Facies are laterally persistent and repeat vertically in successive sequences, allowing environmental variations in seawater chemistry to be distinguished from long-term secular changes. Zircons from a tuff low in the succession have yielded a U–Pb sensitive high-resolution ion microprobe age of 1,492 ± 3 Myr[9]. Our samples were collected from four drill cores (Urapunga 4, 5; Amoco 82/3; Golden Grove 1) (Fig. 1): there were a total of 117 samples—37 from inner-shelf shales, 37 from distal-shelf facies, and 43 from basinal environments, as interpreted[9] using sedimentological criteria.

To investigate the redox chemistry of the Roper seaway, we examined Fe species—including dithionite-extractable Fe (Fe_D), pyrite Fe (Fe_P), HCl-extractable Fe (Fe_H), and total Fe (Fe_T)—in carbonaceous shales. Two ratios, that between highly reactive Fe